GEOPHYSICS, VOL. 81, NO. 2 (MARCH-APRIL 2016); P. C53–C68, 21 FIGS.
10.1190/GEO2014-0586.1

Elastic full-waveform inversion for VTI media: Methodology and sensitivity analysis

Nishant Kamath[1] and Ilya Tsvankin[1]

ABSTRACT

Most existing implementations of full-waveform inversion (FWI) are limited to acoustic approximations. In this paper, we present an algorithm for time-domain elastic FWI in laterally heterogeneous VTI (transversely isotropic with a vertical symmetry axis) media. The adjoint-state method is employed to derive the gradients of the objective function with respect to the stiffness coefficients and then to a chosen set of VTI parameters. To test the algorithm, we introduce Gaussian anomalies in the Thomsen parameters of a homogeneous VTI medium and perform 2D FWI of multicomponent transmission data for two different model parameterizations. To analyze the sensitivity of the objective function to the model parameters, the Fréchet kernel of FWI is obtained by linearizing the elastic wave equation using the Born approximation and employing the asymptotic Green's function. The amplitude of the kernel ("radiation pattern") yields the angle-dependent energy scattered by a perturbation in a certain model parameter. Then we convert the general expressions into simple approximations for the radiation patterns of P- and SV-waves in VTI media. These analytic developments provide valuable insight into the potential of multicomponent elastic FWI and help explain the numerical results for models with Gaussian anomalies in the VTI parameters.

INTRODUCTION

Full-waveform inversion (FWI) is a technique for estimating subsurface properties by using recorded seismic waveforms. Depending on the problem and availability of forward-modeling algorithms, FWI can be performed in the time domain (Gauthier, 1986; Kolb et al., 1986; Mora, 1987; Bunks et al., 1995) or frequency domain (Song and Williamson, 1995; Song et al., 1995; Pratt, 1999; Pratt and Shipp, 1999). Evaluation of the gradient of the objective function is often based on the adjoint-state method, as described in Bamberger et al. (1982), Tarantola (1984a), Fichtner et al. (2006), and Liu and Tromp (2006).

FWI has been extended to anisotropic media, but is applied typically in the acoustic approximation (Plessix and Rynja, 2010; Gholami et al., 2011, 2013; Plessix and Cao, 2011; Shen, 2012). A critical issue for anisotropic FWI is model parameterization. Thomsen notation, widely used in velocity analysis for VTI media, includes the vertical P- and S-wave velocities, V_{P0} and V_{S0}, and the anisotropy coefficients ε, δ, and γ. The anisotropy parameters are often replaced in FWI by the P-wave normal-moveout (NMO) velocity ($V_{\mathrm{nmo}} = V_{P0}\sqrt{1+2\delta}$) and horizontal velocity ($V_{\mathrm{hor}} = V_{P0}\sqrt{1+2\varepsilon}$).

In the case of multiparameter inversion, the results strongly depend on the parameterization and the type of input data (for example, diving waves, near-offset or far-offset reflections). Plessix and Cao (2011) evaluate the sensitivity of the FWI objective function to different parameters by performing singular value decomposition (SVD) of the Fréchet derivative (or "sensitivity") matrix. Another method of analyzing sensitivity is by computing the Fréchet kernel for a point scatterer in the subsurface (Eaton and Stewart, 1994; Prieux et al., 2013; Alkhalifah and Plessix, 2014). The amplitude of the kernel as a function of the scattering angle (called the "radiation pattern") reveals the sensitivity of FWI to a model parameter for a certain range of angles.

Gholami et al. (2013) use finite differences to compute the Fréchet kernel for a point diffractor embedded in a homogeneous acoustic VTI space. An analytic description of the radiation patterns associated with a VTI perturbation in a homogeneous isotropic medium is presented by Alkhalifah and Plessix (2014). They study the radiation patterns for two parameterizations (V_{nmo}, η, δ, and V_{hor}, η, ε; $\eta = (\varepsilon - \delta)/(1+2\delta)$ is the anellipticity coefficient) and conclude that either parameter set can be used when the inversion is carried out with a hierarchic approach.

Plessix and Cao (2011) also perform acoustic FWI of diving waves and small-offset reflection data generated for a synthetic

Manuscript received by the Editor 12 December 2014; revised manuscript received 4 November 2014; published online 18 March 2016.
[1]Colorado School of Mines, Center for Wave Phenomena, Golden, Colorado, USA. E-mail: nkamath@mines.edu; ilya@mines.edu.

VTI model and test different parameterizations with the goal of updating the low-wavenumber component of the model. They show that the combination of V_{nmo}, V_{hor}, and δ provides "slightly better" results than V_{nmo}, η, and δ. Using data from Valhall field, Prieux et al. (2011) update the velocity V_{P0} with acoustic FWI, while keeping ε and δ fixed. These results are used as a benchmark to compare the velocity fields obtained with and without taking anisotropy into account. Warner et al. (2013) estimate V_{P0} by performing 3D acoustic FWI of field data from the North Sea with fixed profiles of ε and δ.

Anisotropic acoustic algorithms, however, do not properly handle reflection amplitudes and cannot be applied to multicomponent data. Elastic FWI of synthetic multicomponent surface data (consisting of both diving waves and reflections) for VTI media is performed by Lee et al. (2010), but suboptimal parameterization in terms of the stiffness coefficients causes ambiguity in their results.

In our previous work (Kamath and Tsvankin, 2013), we invert multicomponent reflection data (PP- and PSV-waves) from a horizontally layered VTI model for the interval Thomsen parameters V_{P0}, V_{S0}, ε, and δ. Although PP-waves alone may be sufficient to resolve V_{P0}, V_{S0}, ε, and δ, stable interval parameter estimation for layers at depth requires employing long-offset data (with the spreadlength-to-depth ratio reaching at least two) or the addition of PS-waves. Inversion of multicomponent data benefits from using a multiscale approach (Bunks et al., 1995), which reduces the sensitivity to the choice of the initial model.

Here, we introduce an extension of elastic FWI to laterally heterogeneous VTI media and study the sensitivity of the inversion to two different sets of model parameters. To compute the gradient of the objective function, we adapt the results of Liu and Tromp (2006) obtained with the adjoint-state method. Sensitivity analysis is performed by deriving the Fréchet kernel for elastic FWI using the Born and WKBJ approximations and an asymptotic representation of the Green's function. The kernel, obtained for arbitrarily anisotropic media, is then used to obtain the radiation patterns for the relevant model parameters. The developed algorithm is applied to transmission data generated for a homogeneous VTI background model with Gaussian anomalies in the Thomsen parameters. The inversion results are explained using the P- and SV-wave radiation patterns for a VTI scatterer.

METHODOLOGY

Full-waveform inversion for VTI media

Time-domain implementations of FWI are designed to minimize the following objective function:

$$\mathcal{F} = \frac{1}{2}\sum_{r=1}^{N} \|\mathbf{u}(\mathbf{x}_r, t) - \mathbf{d}(\mathbf{x}_r, t)\|^2, \tag{1}$$

where N is the number of receivers, $\mathbf{u}(\mathbf{x}_r, t)$ is the data (displacement) computed for a trial model, and $\mathbf{d}(\mathbf{x}_r, t)$ is the displacement recorded at receiver location $\mathbf{x}_r$. Equation 1 implies summation over multiple shots for the same receiver array. Although the relationship between the model and the data is nonlinear, a perturbation in the model is assumed to be linearly related to the perturbation in data:

$$\Delta\mathbf{m} = -\alpha\, \mathbf{J}^T \Delta\mathbf{d}, \tag{2}$$

where $\mathbf{J}$ is the Fréchet derivative matrix, T denotes transposition, and $\Delta\mathbf{d}$ is the perturbation in the data. The model update $\Delta\mathbf{m}$ is computed as the gradient of the objective function, $\mathbf{J}^T\Delta\mathbf{d}$, scaled by the coefficient α (which can be found from line search).

If the number of unknowns is relatively small (as for layered VTI media studied by Kamath and Tsvankin, 2013), the Fréchet matrix can be computed explicitly by perturbing each model parameter, which makes it possible to update the model using equation 2.

Application of the adjoint-state method

Computation of the Fréchet derivatives for laterally heterogeneous media becomes prohibitively expensive because it involves calculating as many forward models at each iteration as the number of parameters (typically defined on a grid). Hence, instead of using equation 2 it is more practical to calculate the gradient ($\mathbf{J}^T\Delta\mathbf{d}$ in equation 2) of the objective function with the adjoint-state method, which has been widely used in FWI (Tarantola, 1984b; Fichtner et al., 2006; Liu and Tromp, 2006; Plessix, 2006). The model update, which is a scaled version of the gradient, is then calculated using steepest-descent or conjugate-gradient algorithms. Alternatively, either the so-called BFGS (Broyden-Fletcher-Goldfarb-Shanno) method or its limited-memory equivalent, the L-BFGS method (both are quasi-Newton techniques), can be employed to scale the gradient by the inverse of an approximate Hessian matrix (Pratt et al., 1998; Virieux and Operto, 2009).

The adjoint-state method is designed to compute the gradient of the objective function using the so-called "adjoint wavefield." Because the variable-density elastic wave equation is self-adjoint, it can be solved for the adjoint wavefield with the data residuals treated as sources (see Appendix A). The residuals at each time step are injected "backward in time" (i.e., starting from the last time sample), which is commonly described as back-propagation of data residuals. For 2D multicomponent data, the vertical and horizontal displacement components of the data residuals should be injected into the medium simultaneously. The gradient computation, as shown in Appendix A, involves applying the imaging condition to the spatial derivatives of the forward and adjoint wavefields.

Here, we assume that the properties of the VTI medium vary in 2D and consider only in-plane polarized waves (P and SV). Hence, the model is described by four stiffness coefficients (written in the Voigt notation): C_{11}, C_{33}, C_{13}, and C_{55}. However, description of wave propagation and inversion of seismic data can be facilitated by employing Thomsen parameters and their combinations (e.g., the anellipticity coefficient η, Alkhalifah and Tsvankin, 1995). Lee et al. (2010), who parameterize the VTI model in terms of the stiffnesses, are unable to resolve the coefficient C_{13}, likely because of the tradeoff between C_{13} and C_{55} in P-wave kinematic signatures (Tsvankin, 2012).

Kamath and Tsvankin (2013) could constrain the relevant Thomsen parameters (V_{P0}, V_{S0}, ε, and δ), although the algorithm operated with the vertical velocities of P- and S-waves and the P-wave NMO and horizontal velocities. Here we define the model either in terms of the velocities V_{P0}, V_{S0}, V_{nmo}, and V_{hor} (parameterization I) or using $\ln(1/V_{P0}^2)$, $\ln(1/V_{S0}^2)$, $(1+2\varepsilon)$, and $(1+2\delta)$ (parameterization II). The latter combination is an extension of Shen's (2012) parameterization to elastic media; also, in contrast to Shen

(2012), we update the coefficient δ during the inversion rather than keeping it fixed.

The gradients of the objective function (equation 1) with respect to the elements of the stiffness tensor are derived in Appendix A using the results of Liu and Tromp (2006):

$$\frac{\partial \mathcal{F}}{\partial c_{ijkl}} = -\int_0^T \frac{\partial u_i}{\partial x_j}\frac{\partial \psi_k}{\partial x_l}\,dt, \tag{3}$$

where $\mathbf{u}$ and $\boldsymbol{\psi}$ are the forward and adjoint displacement wavefields, respectively. Using the chain rule, we can find the gradient for each model parameter m_n:

$$\frac{\partial \mathcal{F}}{\partial m_n} = \sum_{ijkl}\frac{\partial \mathcal{F}}{\partial c_{ijkl}}\frac{\partial c_{ijkl}}{\partial m_n}. \tag{4}$$

The stiffness coefficients are expressed in terms of the velocities (V_{P0}, V_{S0}, V_{nmo}, and V_{hor}) in equations A-18–A-21. Combining equations 3, 4, and A-18–A-21 yields the gradients for parameterization I (equations A-22–A-25). In a similar manner, we derive the gradients for parameterization II (equations A-30–A-33).

FWI is implemented here in the time domain and the model is updated using the steepest-descent method combined with a parabolic line-search algorithm. The same step length is used for all medium parameters.

Radiation patterns for elastic FWI

To obtain expressions for radiation patterns produced by a scatterer in the subsurface, we consider an elastic, anisotropic homogeneous background medium with spatially varying perturbations in the stiffness coefficients. It should be emphasized that the perturbed stiffnesses correspond to an arbitrarily anisotropic medium. Afterwards, we obtain relatively simple expressions for the radiation patterns assuming the background to be isotropic and the perturbations to have VTI symmetry.

General expressions

Following Calvet et al. (2006) and Alkhalifah and Plessix (2014), we represent the elastic wave equation for a perturbation δc_{ijkl} in the stiffness tensor using the Born approximation:

$$\rho\frac{\partial^2(\delta u_i)}{\partial t^2} - \frac{\partial}{\partial x_j}\left(c_{ijkl}\frac{\partial(\delta u_k)}{\partial x_l}\right) = \frac{\partial}{\partial x_j}\left(\delta c_{ijkl}\frac{\partial u_k}{\partial x_l}\right), \tag{5}$$

where $\delta\mathbf{u}$ is the corresponding perturbation in the wavefield, and ρ is the density. The solution of equation 5 can be expressed in terms of the Green's functions G_{mk} and G_{ni} (Appendix B):

$$\delta u_n(\mathbf{x}_r,\omega) = -\int_{V(\mathbf{x}')} f_m(\mathbf{x}_s,\omega)\;\delta c_{ijkl}(\mathbf{x}') \times \frac{\partial G_{mk}(\mathbf{x}_s,\mathbf{x}',\omega)}{\partial x_l'}\frac{\partial G_{ni}(\mathbf{x}_r,\mathbf{x}',\omega)}{\partial x_j'}\,dV(\mathbf{x}'), \tag{6}$$

where $\mathbf{x}_s$ and $\mathbf{x}_r$ are the locations of the source and receiver, respectively, $\mathbf{f}$ is the density of body forces, and $V(\mathbf{x}')$ is the volume that includes all scatterers $\mathbf{x}'$. The Green's functions are then replaced by their asymptotic representation (Vavryčuk, 2007). Taking the spatial derivative of just the exponent of $\mathbf{G}$ (i.e., of its rapidly varying part, according to the WKBJ approximation) yields (equation B-13):

$$\delta u_n(\mathbf{x}_r,\omega) = \int_{V(\mathbf{x}')} f_m(\mathbf{x}_s,\omega)\mathcal{A}(\omega)p_l^s\;p_j^r\;g_k^s\;g_i^r\;\delta c_{ijkl}\;dV(\mathbf{x}'). \tag{7}$$

Here, the superscripts s and r denote the source (incident) and receiver (scattered) wavefields, respectively, $\mathcal{A}(\omega)$ is a function of frequency and the background velocities for the incident and scattered wavefields (equation B-14), and $\mathbf{p}$ and $\mathbf{g}$ are the unit slowness and polarization vectors, respectively. The radiation pattern is the amplitude of the kernel in equation 7 that varies with the incidence and scattering angles. For a model parameterized in terms of the stiffnesses, the radiation pattern derived from equation 7 is (equation B-15):

$$\Omega = p_l^s\;p_j^r\;g_k^s\;g_i^r. \tag{8}$$

Equation 8 is valid for a perturbation δc_{ijkl} corresponding to an elastic, arbitrarily anisotropic scatterer in 3D. In this study, however, we consider the in-plane polarized waves (P and SV) in a 2D elastic VTI medium, so the indices i, j, k, and l in equations 6–8 take values of 1 and 3.

Application to VTI media

In Appendix B, we use equation 8 to obtain explicit expressions for the radiation patterns in VTI media. The normalized scattering coefficients for the P- and SV-wavefields for parameterization I are given by equations B-16–B-19 and B-20–B-23, respectively. In the case of the transmitted wavefield, the incidence and scattering angles coincide. Substituting equations B-24–B-31 into equations B-16–B-23, we obtain the following radiation patterns (normalized by $4\rho V_{P0}$) for the scattered P-wavefield:

$$\Omega^P(V_{P0}) = \cos^2\theta, \tag{9}$$

$$\Omega^P(V_{S0}) = 0, \tag{10}$$

$$\Omega^P(V_{\mathrm{nmo}}) = \frac{1}{4}\sin^2 2\theta, \tag{11}$$

$$\Omega^P(V_{\mathrm{hor}}) = \sin^4\theta, \tag{12}$$

where θ is the incidence angle. The patterns for the scattered SV-wavefield (normalized by $2\rho V_{P0}$) are:

$$\Omega^S(V_{P0}) = 0, \tag{13}$$

$$\Omega^S(V_{S0}) = -2\frac{V_{S0}}{V_{P0}}, \tag{14}$$

$$\Omega^S(V_{\mathrm{nmo}}) = \frac{1}{2}\sin^2 2\theta, \tag{15}$$

$$\Omega^S(V_{\rm hor}) = \frac{1}{2}\sin^2 2\theta. \qquad (16)$$

The absolute values (magnitude) of the radiation patterns in Figure 1 show how perturbations in the velocities V_{P0}, $V_{\rm nmo}$, and $V_{\rm hor}$ scatter P-wave energy for different incidence angles. In our approximation, a perturbation in V_{S0} does not influence the scattered P-wavefield. As expected, the intensity of the wavefield scattered by a perturbation in V_{P0} reaches its maximum for propagation along the symmetry axis and goes to zero in the orthogonal (isotropy) plane (Figure 1a). In contrast, a perturbation in $V_{\rm hor}$ produces the largest scattering in the isotropy plane, with a rapid decay toward the symmetry axis (Figure 1c). The maximum energy scattered by a perturbation in $V_{\rm nmo}$ is four times smaller than that for V_{P0} and corresponds to an angle of 45° with the symmetry axis (Figure 1b).

A perturbation in V_{S0} scatters the SV-wavefield uniformly for the entire range of incidence angles (Figure 2a), which is likely due to the fact that V_{S0} also represents the horizontal SV-wave velocity. The radiation patterns of $V_{\rm nmo}$ and $V_{\rm hor}$ (Figure 2b and 2c, respectively) for SV-waves are similar to that of $V_{\rm nmo}$ for the P-wave (Figure 1b). The SV-wave is primarily influenced by V_{S0} and the parameter $\sigma=(V_{P0}/V_{S0})^2(\varepsilon-\delta)=(V_{\rm hor}^2-V_{\rm nmo}^2)/(2V_{S0}^2)$ (Tsvankin, 2012). Therefore, for a model described in terms of V_{P0}, V_{S0}, $V_{\rm nmo}$, and $V_{\rm hor}$, the SV-wavefield is weakly dependent on the velocity V_{P0}. This explains why a perturbation in V_{P0} does not scatter SV-waves (equation 13).

The P-wave radiation patterns for the velocities V_{P0}, $V_{\rm nmo}$, and $V_{\rm hor}$ are centered at angles 0°, 45°, and 90°, respectively, which mitigates the trade-off in the scattered energy for this parameterization. These radiation patterns can be used to qualitatively predict those for other parameterizations. For instance, if the model is described by the Thomsen parameters V_{P0}, ε, and δ, anomalies in both V_{P0} and δ should be responsible for the scattered energy near 45° because $V_{\rm nmo} = V_{P0}\sqrt{1+2\delta}$. Similarly, one would expect anomalies in both V_{P0} and ε to contribute to scattering near the isotropy plane, as $V_{\rm hor} = V_{P0}\sqrt{1+2\varepsilon}$.

Because the scattered SV-wavefield is not sensitive to V_{P0}, the SV-wave radiation patterns for ε and δ have the same shape as those for $V_{\rm hor}$ and $V_{\rm nmo}$, respectively. By making similar arguments, it is possible to deduce the general behavior of the radiation patterns for other parameterizations, such as the ones discussed in Gholami et al. (2013) and Alkhalifah and Plessix (2014). Note that the radiation patterns of V_{P0}, $V_{\rm nmo}$, and $V_{\rm hor}$ for the transmitted P-wavefield in

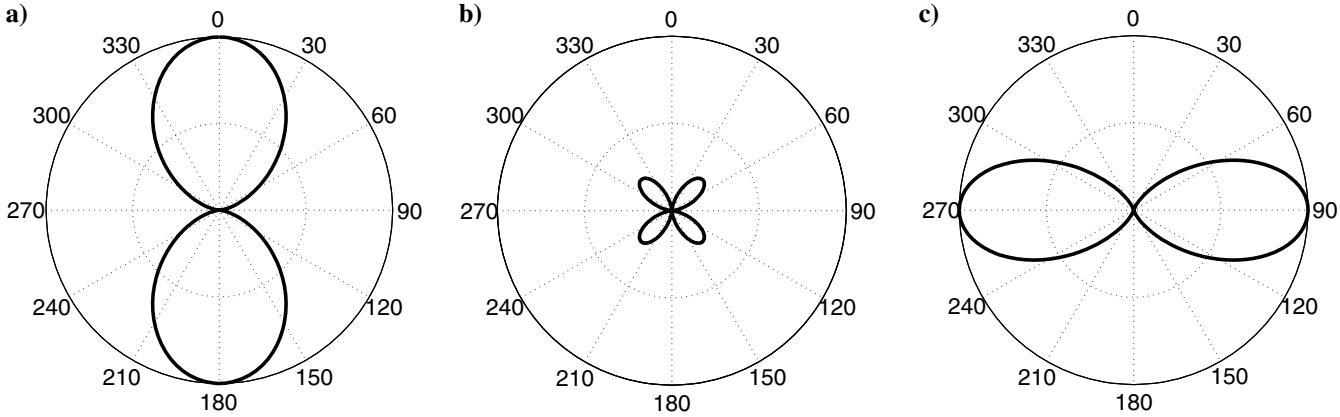

Figure 1. Radiation patterns of the velocities (a) V_{P0}, (b) $V_{\rm nmo}$, and (c) $V_{\rm hor}$ computed from equations 9, 11, and 12 (respectively) for the P-wavefield. The VTI perturbations are inserted into a homogeneous isotropic background.

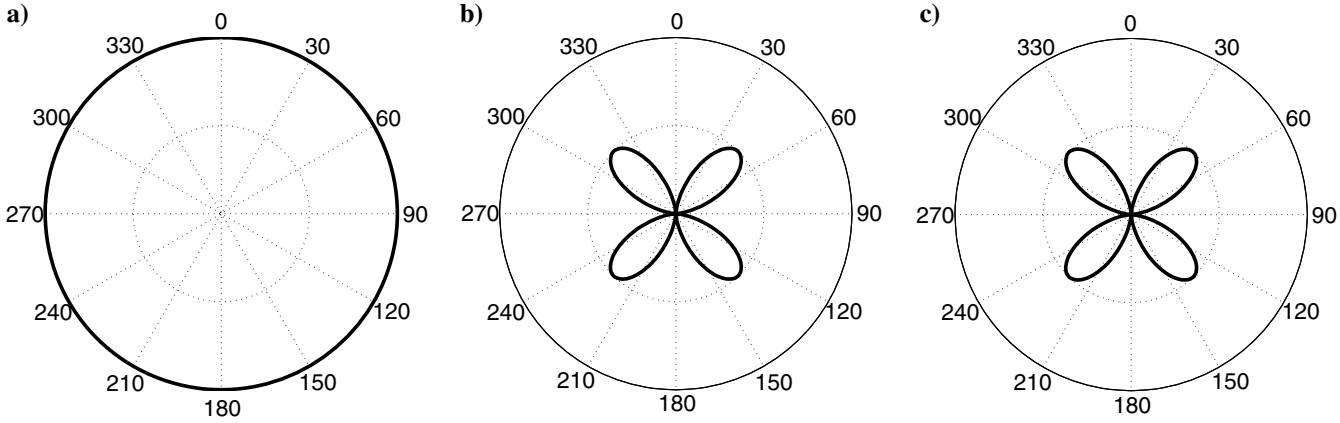

Figure 2. Radiation patterns of the velocities (a) V_{S0}, (b) $V_{\rm nmo}$, and (c) $V_{\rm hor}$ computed from equations 14, 15, and 16 (respectively) for the S-wavefield. The VTI perturbations are inserted into a homogeneous isotropic background; the ratio $V_{S0}/V_{P0} = 0.5$.

elastic media are identical to those obtained for acoustic media. Elastic FWI, however, also includes SV-waves, which help estimate the velocity V_{S0} and better constrain the other parameters.

The P-wave radiation patterns (normalized by ρV_{P0}^2) for parameterization II, obtained analogously to those for parameterization I, are:

$$\Omega^P(\ln(1/V_{P0}^2)) = -1, \tag{17}$$

$$\Omega^P(\ln(1/V_{S0}^2)) = 0, \tag{18}$$

$$\Omega^P(1+2\varepsilon) = \sin^4\theta, \tag{19}$$

$$\Omega^P(1+2\delta) = \frac{1}{4}\sin^2 2\theta. \tag{20}$$

For the scattered S-wavefield (normalized by $\rho V_{P0}^2/4$), we find:

$$\Omega^S(\ln(1/V_{P0}^2) = 0, \tag{21}$$

$$\Omega^S(\ln(1/V_{S0}^2) = -4\frac{V_{S0}^2}{V_{P0}^2}, \tag{22}$$

$$\Omega^S(1+2\varepsilon) = \sin^2 2\theta, \tag{23}$$

$$\Omega^S(1+2\delta) = -\sin^2 2\theta. \tag{24}$$

Here, the velocities are normalized by 1 km/s. The P- and S-wave radiation patterns for parameterization II, computed from equations 17–24, are plotted in Figures 3 and 4. These patterns generally confirm the above arguments regarding the sensitivity analysis in terms of Thomsen parameters. For example, the radiation patterns of the parameters $1+2\varepsilon$ and $1+2\delta$ for both P- and SV-waves have the same shape as those for V_{hor} and V_{nmo} obtained for parameterization I.

The radiation patterns do not change if the velocities (or their squares) are used instead of the logarithm of the squared slownesses. However, we prefer to employ the logarithm for two reasons: (a) to make the parameters dimensionless, with the same order of magnitude as that of the anisotropy coefficients (because we do not have an inverse Hessian scaling the gradient), and

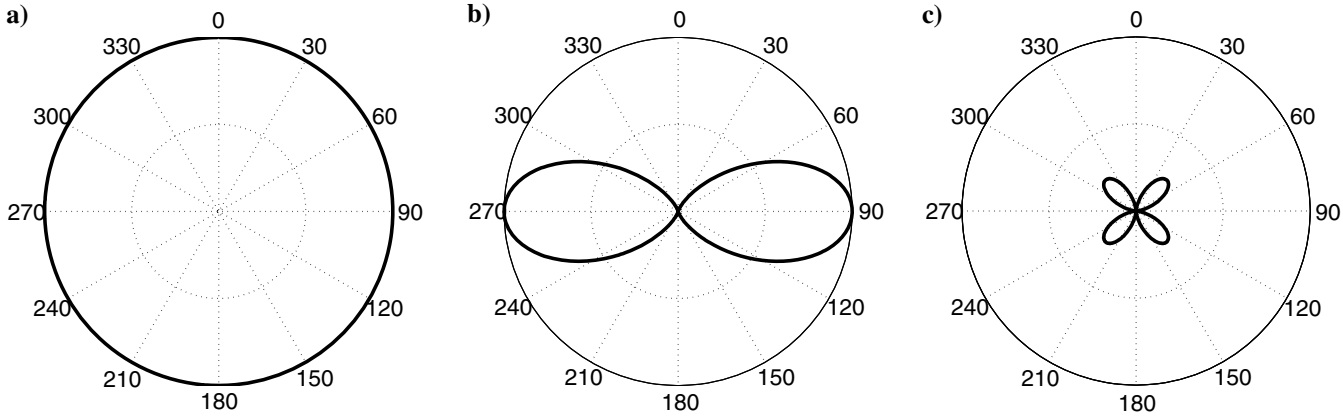

Figure 3. Radiation patterns of the parameters (a) $\ln(1/V_{P0}^2)$, (b) $1+2\varepsilon$, and (c) $1+2\delta$ computed from equations 17, 19, and 20 (respectively) for the P-wavefield.

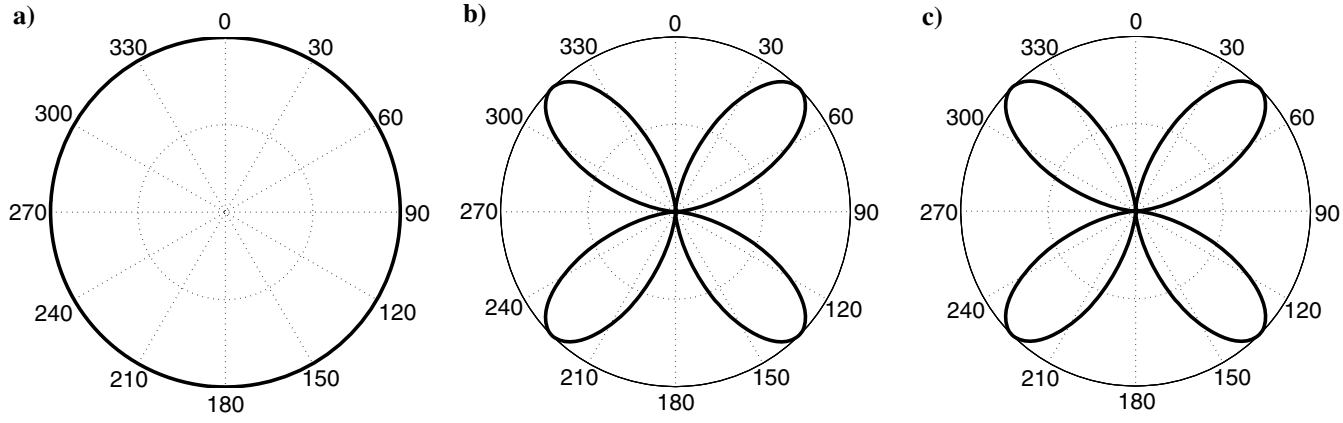

Figure 4. Radiation patterns of the parameters (a) $\ln(1/V_{S0}^2)$, (b) $1+2\varepsilon$, and (c) $1+2\delta$ computed from equations 22, 23, and 24 (respectively) for the S-wavefield. The ratio $V_{S0}/V_{P0} = 0.5$.

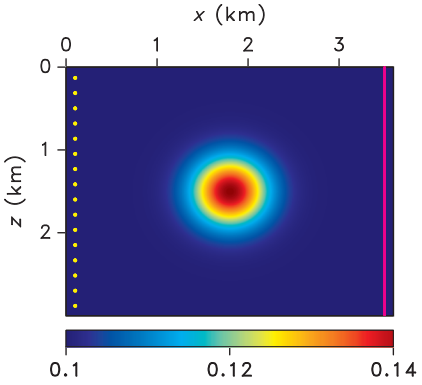

Figure 5. VTI model with a Gaussian anomaly (standard deviation $\sigma = 300$ m) in the anisotropy parameter ε. The background and maximum values of ε are 0.1 and 0.142, respectively. The other Thomsen parameters are spatially invariant: $V_{P0} = 3000$ m/s, $V_{S0} = 1500$ m/s, and $\delta = -0.05$. The dots on the left mark the source locations and the vertical line on the right represents an array of receivers placed at each grid point (6.6 m apart). The wavefields are generated by horizontal displacement sources.

(b) Shen (2012) showed that the logarithm-based parameterization may lead to faster convergence. Note that an anomaly in $\ln(1/V_{P0}^2)$ scatters P-wave energy uniformly in all directions (Figure 3a), which means that updates in V_{P0} are independent of the source-receiver configuration.

Parameterization I yields radiation patterns that are more "orthogonal" (have less overlap), but this also restricts the range of wavenumbers that can be recovered by FWI (e.g., one can obtain only low-wavenumber updates for V_{hor}). The second parameterization has a velocity (V_{P0}) which has a more "isotropic" radiation pattern. This helps retrieve a wider range of wavenumbers for V_{P0}, but creates trade-offs between V_{P0} and the anisotropy coefficients.

ANALYSIS OF FWI OF TRANSMISSION DATA

Next, we perform tests for simple synthetic models to verify the accuracy of the gradient computation and of the inversion algorithm as a whole. In addition, we employ the analytic expressions for radiation patterns obtained above to explain the inversion results. Because the initial stage of FWI typically involves diving waves, the

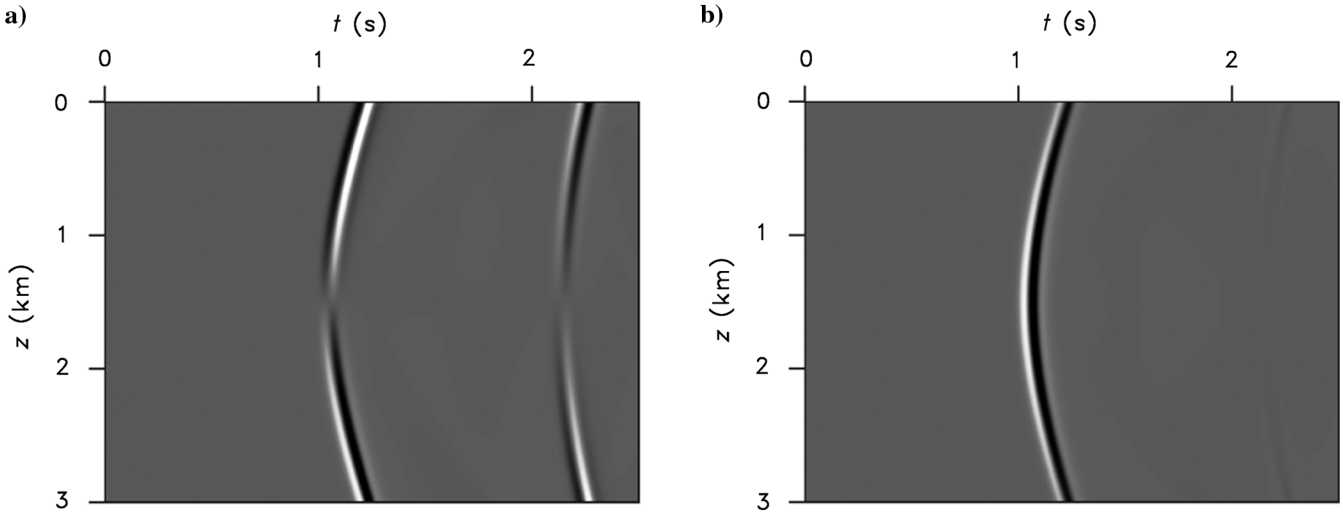

Figure 6. (a) Vertical and (b) horizontal displacements for the model in Figure 5 generated by a shot at $z = 1.5$ km.

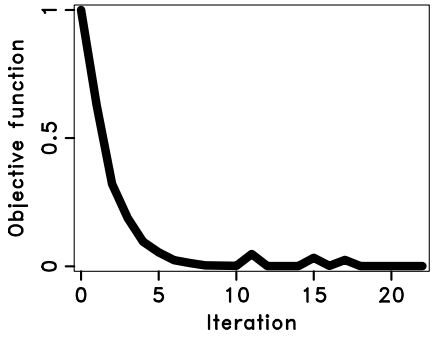

Figure 7. Change in the normalized objective function with iterations for the model from Figure 5.

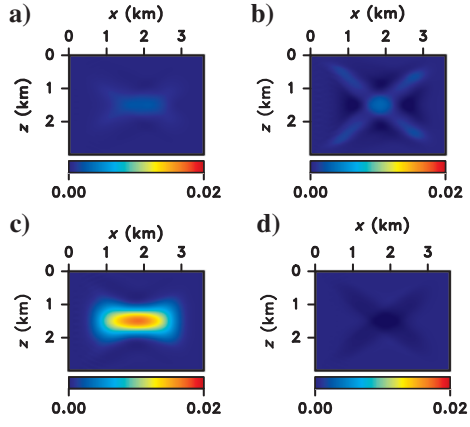

Figure 8. Fractional difference between the estimated and initial (background) parameters (a) V_{P0} and (b) V_{S0} for the model from Figure 5. The difference between the estimated and initial parameters (c) ε and (d) δ for the same model.

data are generated for transmission experiments. The model includes Gaussian anomalies in the Thomsen parameters V_{P0}, V_{S0}, and ε inserted into a homogeneous VTI background between line arrays of sources and receivers.

The set of tests in Figures 5–18 is performed for parameterization I (V_{P0}, V_{S0}, V_{hor}, and V_{nmo}). In the first test, the model includes an anomaly in ε, while the other parameters are spatially invariant (Figure 5). The wavefield is generated by a point displacement source polarized in the horizontal direction with a peak frequency of 10 Hz. The vertical and horizontal displacements ("recorded data") from a shot in the center of the array are shown in Figure 6. The "modeled" data are then generated in the background medium without the anomaly, and the adjoint source is obtained as the difference between the two wavefields.

Starting from the homogeneous background model, we perform the inversion using the steepest-descent method. We run up to 50 iterations and terminate the inversion if the objective function flattens out earlier (Figure 7). The inverted and initial values of V_{P0} and δ are close, which confirms that FWI converges toward the actual model. The updates in V_{hor}, combined with negligible changes in V_{P0}, ensure the reconstruction of the anomaly in ε (Figure 8).

These results are well explained by the radiation patterns in Figure 1. For this source-receiver geometry, the aperture is about 41° on both sides of the isotropy (horizontal) plane. The amplitude of the energy scattered by V_{hor} reduces by 50% at an angle of about $\pm 33^{\circ}$ from the horizontal (Figure 1c), so the radiation pattern of V_{hor} is largely decoupled from those of V_{P0}, V_{S0}, and V_{nmo}. Therefore, FWI updates only the horizontal velocity, which results in an appropriate change in the coefficient ε and an accurate inverted model.

Even though the objective function decreases to just 0.04% of the initial value, there is a small error in ε: the maximum estimated ε is about 0.12, whereas the actual value is 0.14. The shape of the anomaly is somewhat distorted (i.e., it is stretched along the horizontal axis) because of the source-receiver configuration. For this acquisition geometry, spatial resolution should indeed be higher in the vertical direction than horizontally, as discussed by Wu and Toksöz (1987). When the aperture is increased to about 51° on both sides of the isotropy plane (Figure 9), the shape of the anomaly is better resolved (Figure 10). In addition, because the inverted velocities are closer to the actual values, the estimated ε (maximum value of 0.13) is slightly more accurate than in the previous example. This configuration, which yields better inversion results, is used in all subsequent tests.

Next, we introduce an anomaly in the P-wave vertical velocity V_{P0}, with the sources still polarized horizontally (Figure 11). The anomaly in V_{P0} also causes perturbations in the NMO and horizontal velocities. The largest update (about 74% of the actual anomaly) for the given configuration is the one for the velocity V_{hor}, whereas the updates for V_{P0} (45%) and V_{nmo} (44%) are much smaller. A comparison of the observed displacement and that computed for the inverted model indicates that the data misfit is relatively small. Most likely, the search is trapped in a local minimum because of the complexity of the multicomponent wavefield. In a later test we show that it is possible to obtain much better results for the same configuration when the wavefield includes only P-waves. Not only is the inversion unable to recover the true anomaly in V_{P0} (Figure 12a), an update in V_{hor} without the cor-

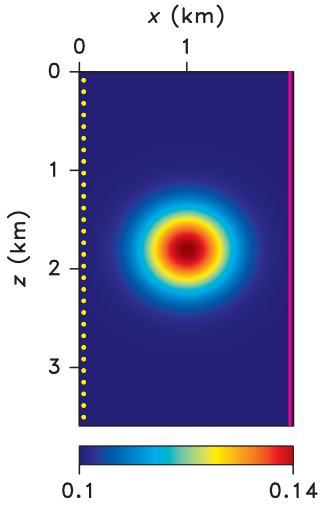

Figure 9. VTI model with the same parameters as in Figure 5, but the source and receiver arrays are extended vertically by 0.6 km and the distance between them is reduced from 3.4 to 1.92 km. The wavefields are generated by horizontal displacement sources.

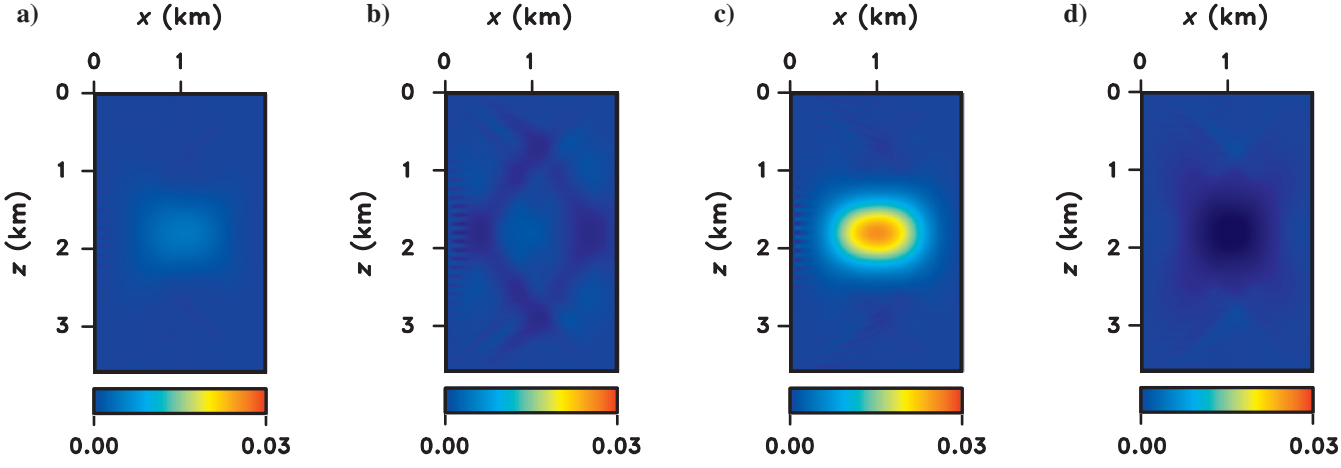

Figure 10. Fractional difference between the estimated and initial parameters (a) V_{P0} and (b) V_{S0} for the model from Figure 9. The difference between the estimated and initial parameters (c) ε and (d) δ for the same model.

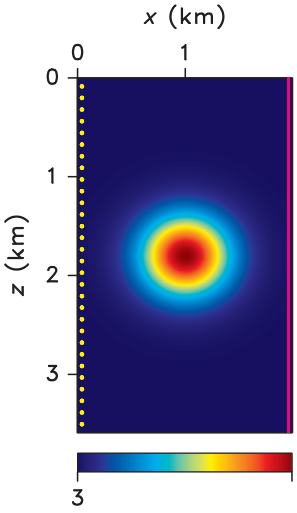

Figure 11. VTI model with a Gaussian anomaly in V_{P0}. The background and maximum values of V_{P0} are 3000 m/s and 3283 m/s, respectively. The other Thomsen parameters are spatially invariant: $V_{S0} = 1500$ m/s, $\delta = -0.05$, and $\varepsilon = 0.1$. The wavefields are generated by horizontal displacement sources.

responding change in V_{P0} results in an undesired update in ε (Figure 12c). Because the parameter δ depends on the velocity ratio V_{nmo}/V_{P0}, and the inversion updates both the velocities proportionately, there is no significant change in δ (Figure 12d).

When the source and receiver arrays for the same model are rotated by 90° (Figure 13), the inversion algorithm predominantly updates V_{P0} (Figure 14a). Because the receivers do not record most of the energy scattered by the anomalies in V_{nmo} and V_{hor} (Figure 1), the algorithm does not update these parameters. Hence, although the anomaly in V_{P0} is recovered, the parameters ε and δ, which depend on V_{hor} and V_{nmo}, are distorted (Figure 14c and 14d, respectively).

Another test is performed for a Gaussian anomaly in V_{S0} embedded between vertical source and receiver arrays (Figure 15). The maximum perturbation in V_{S0} with respect to the background is the same as that for V_{P0} in a previous test (Figure 11), but the percentage perturbation in V_{S0} is two times higher. Hence, to avoid the problem of cycle-skipping, the peak frequency of the source is reduced to 5 Hz. The inversion results, obtained using both P- and S-waves, include an update only in V_{S0} (Figure 16), which indicates no apparent trade-off between the model parameters. As was the case in the inversion for ε, despite the significant decrease in the

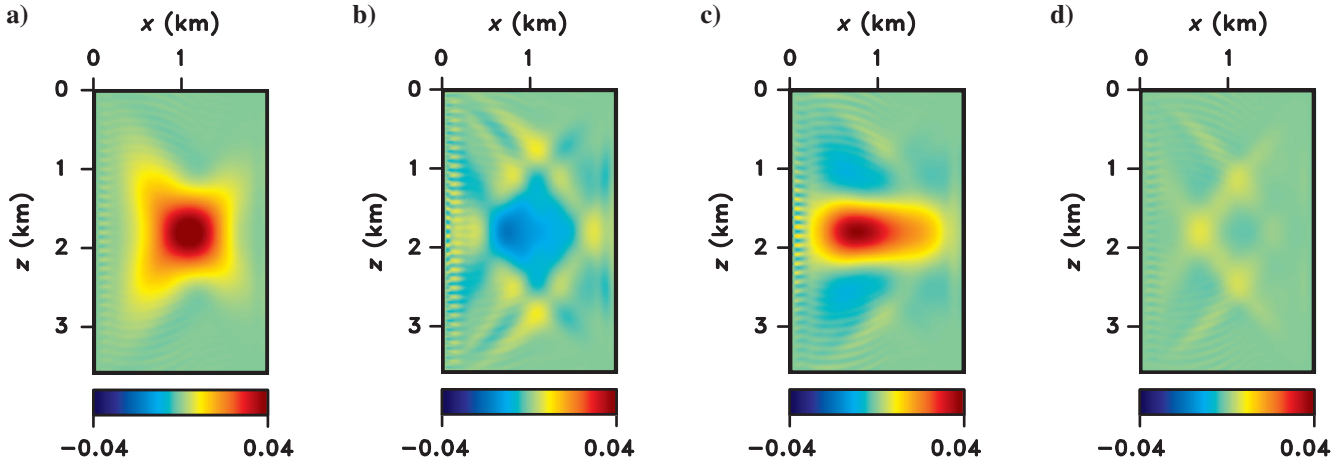

Figure 12. Fractional difference between the estimated and initial parameters (a) V_{P0} and (b) V_{S0} for the model from Figure 11. The difference between the estimated and initial parameters (c) ε and (d) δ for the same model.

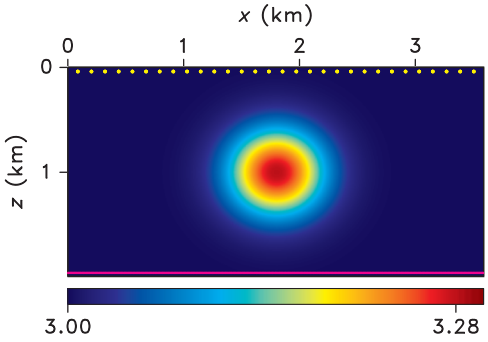

Figure 13. VTI model with a Gaussian anomaly in V_{P0}. The source and receiver arrays are horizontal. The wavefields are generated by vertical displacement sources.

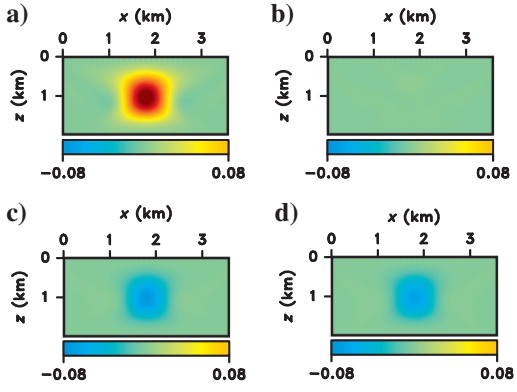

Figure 14. Fractional difference between the estimated and initial parameters (a) V_{P0} and (b) V_{S0} for the model from Figure 13. The difference between the estimated and initial parameters (c) ε and (d) δ for the same model.

objective function (to 0.03% of the initial value), the estimated V_{S0} is off by about 3%. Interestingly, the inversion for V_{S0} yields similar results when the source and receiver arrays are horizontal and wave propagation is predominantly vertical, likely because the V_{S0} anomaly scatters the SV-waves equally in all directions (Figure 2a).

It is important to test the inversion algorithm on data consisting only of either P- or SV-waves. After generating the complete wavefield for the model from Figure 11, we mask the S-wave arrivals. The shear data are also removed from the wavefield modeled at each iteration during the inversion, so the objective function contains the difference of the P-waveforms only. Note that although the adjoint sources include only the P-wave residuals, the adjoint wavefield contains both the P- and S-wavefields. Still, because the modeled and observed data are missing S-waves, the gradients are dominated by the P-wave events. As a result, the objective function becomes less complex and the inversion converges more rapidly (Figure 17).

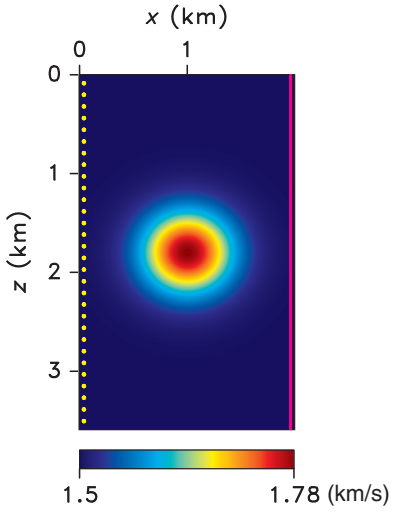

Figure 15. VTI model with a Gaussian anomaly in V_{S0}. The background and maximum values of V_{S0} are 1500 m/s and 1783 m/s, respectively. The other Thomsen parameters are spatially invariant: $V_{P0} = 3000$ m/s, $\delta = -0.05$, and $\varepsilon = 0.1$. The wavefields are generated by vertical displacement sources.

Furthermore, removing S-waves increases the accuracy of the inversion for the anomaly in V_{P0} (compare Figures 18 and 12). Kamath and Tsvankin (2013) made a similar observation: operating with just PP data generally improved the convergence of FWI and the objective function seemingly became more quadratic. Note, however, that P-wave transmission data alone cannot constrain the velocity V_{S0}. Also, for more complex models, SV-waves should help better constrain the parameters V_{P0}, V_{nmo}, and V_{hor}.

Next, we mask the P-wave arrivals in both the observed and modeled data to determine the contribution of the shear wavefield to the inversion for an anomaly in ε (Figure 9). Although the adjoint wavefield contains both the P- and S-wavefields, in this case, the gradients (and, therefore, the inversion) are dominated by the SV-wave energy. FWI of SV-waves increases ε by only 25% of the desired update (plots for this test are not shown), whereas the joint inversion of P- and SV-waves produced a much more accurate result (Figure 10). In addition, there is a decrease in the value of δ, which clearly indicates the trade-off between the two parameters. Therefore, estimation of ε is primarily based on the information provided by P-waves.

Finally, we use parameterization II to recover the anomalies in ε, V_{P0}, and V_{S0} (Figures 9, 11, and 15, respectively). For the anomaly in ε (Figure 9), the results are close to those for parameterization I: the ε-field is well recovered, but the trade-off between V_{P0} and ε causes a small erroneous update in V_{P0}. The second parameterization, however, provides an improvement in the inversion results (Figure 19) for the anomaly in V_{P0} (Figure 11). Because the radiation pattern of $\ln(1/V_{P0}^2)$ is uniform (Figure 3a), a larger fraction of energy scattered by that parameter is recorded by the receivers. Hence, the update in V_{P0} is close to the desired value (9%), although the trade-off between V_{P0} and ε results in a slight distortion in the latter parameter (Figure 19c). The nonlinearity of the inversion (likely at least partially caused by the presence of shear-wave data) manifests itself in the oscillations in the objective function (Figure 20).

The radiation patterns of $\ln(1/V_{S0}^2)$ (parameterization II) and V_{S0} (parameterization I) are identical, so the shear-wave vertical velocity (e.g., for the model in Figure 15) is resolved equally well with both parameterizations.

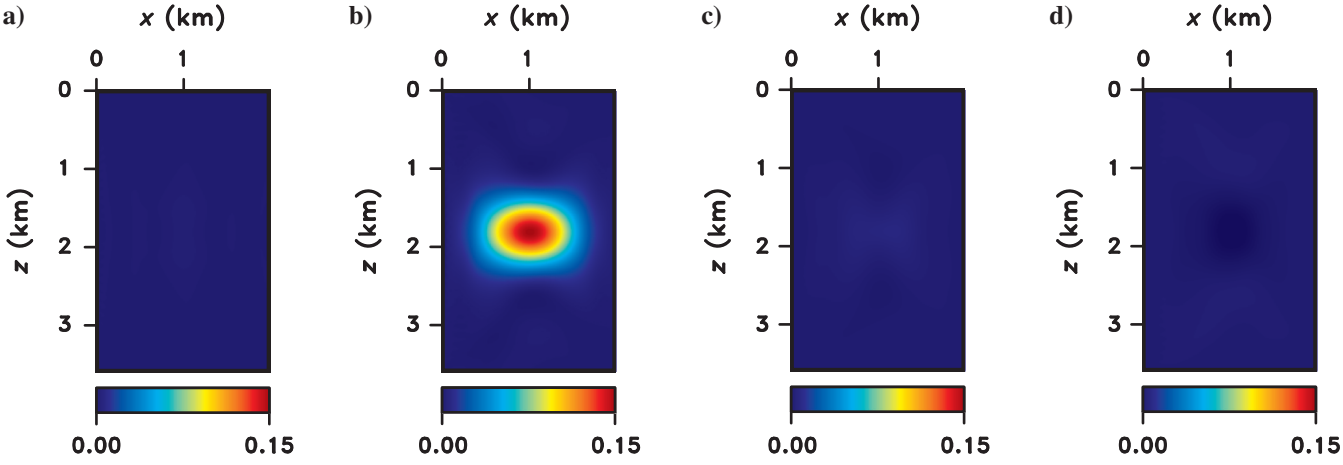

Figure 16. Fractional difference between the estimated and initial parameters (a) V_{P0} and (b) V_{S0} for the model from Figure 15. The difference between the estimated and initial parameters (c) ε and (d) δ for the same model.

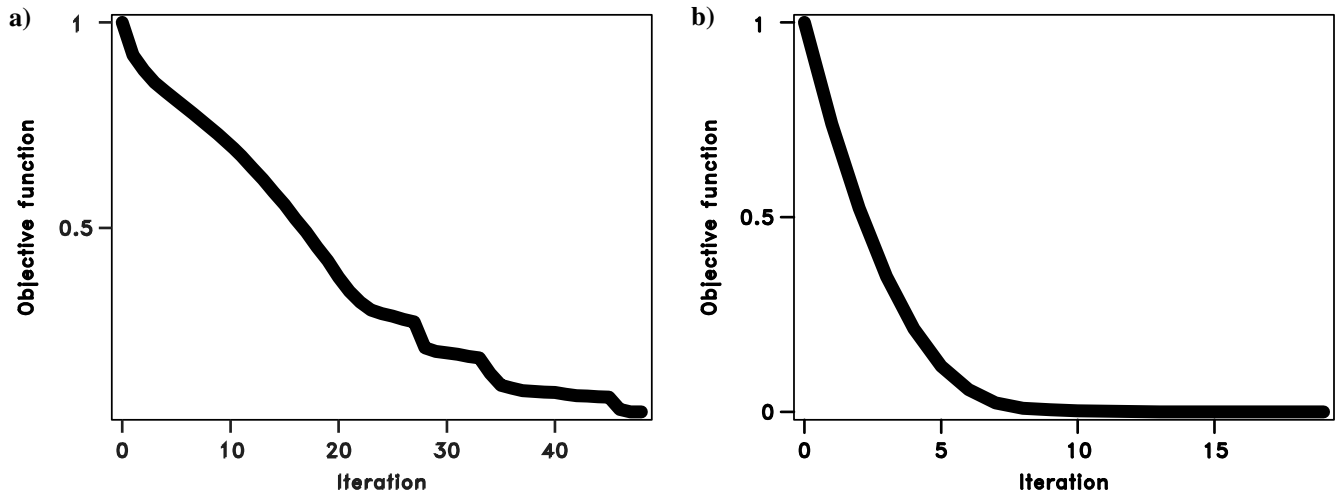

Figure 17. Change in the normalized objective function with iterations for the model from Figure 11 when the data (a) consist of both the P- and S-wave arrivals and (b) contain only the P-waves.

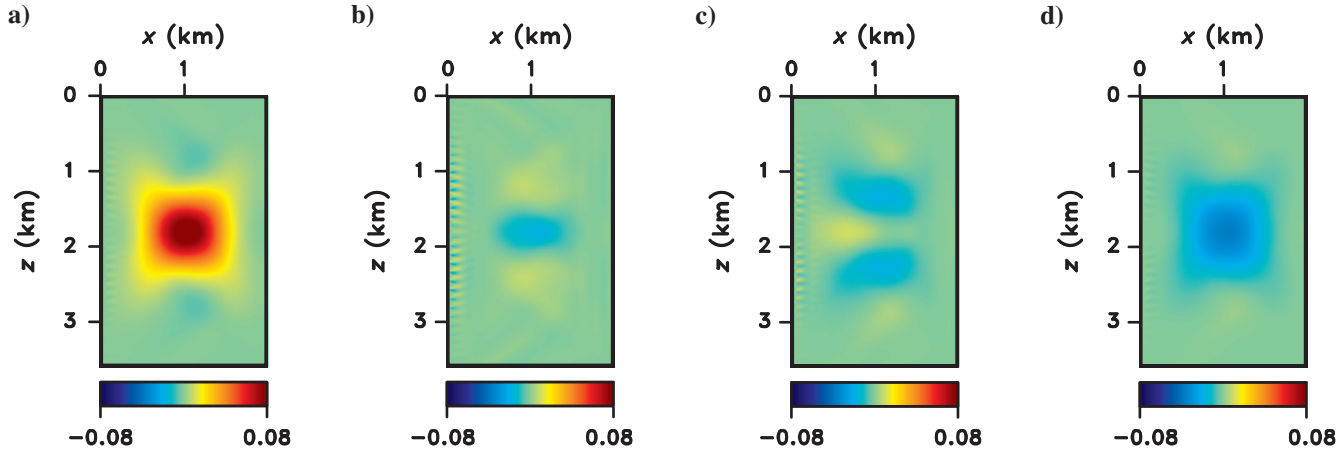

Figure 18. Fractional difference between the estimated and initial parameters (a) V_{P0} and (b) V_{S0} for the model from Figure 11 when the objective function is calculated using only the P-wave data. The difference between the estimated and initial parameters (c) ε and (d) δ for the same model.

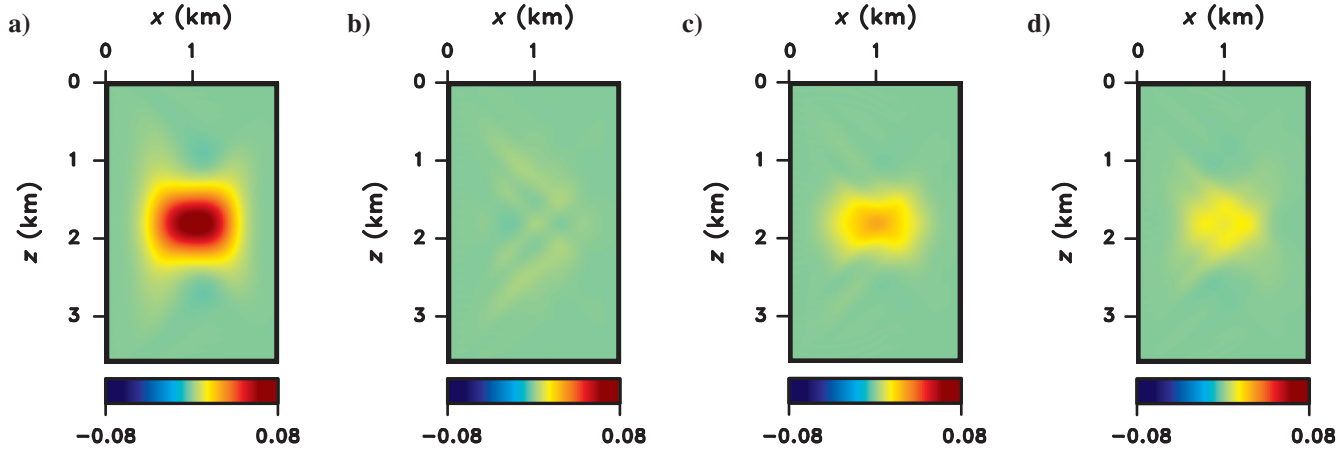

Figure 19. Inversion results obtained with parameterization II. Fractional difference between the estimated and initial parameters (a) V_{P0} and (b) V_{S0} for the model from Figure 11. The difference between the estimated and initial parameters (c) ε and (d) δ for the same model.

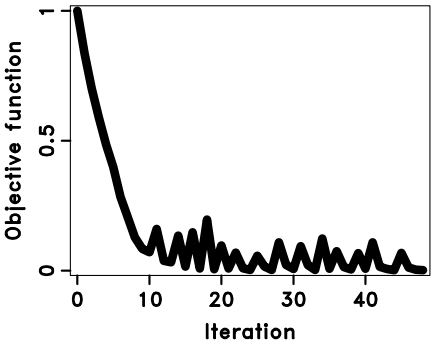

Figure 20. Change in the normalized objective function with iterations for the model from Figure 11. The function is computed using parameterization II.

CONCLUSIONS

We presented a framework for time-domain full-waveform inversion of multicomponent data from elastic VTI media and discussed sensitivity analysis for different model parameterizations. The method of Lagrange multipliers was employed to compute the gradient of the objective function with respect to the stiffness coefficients for an arbitrarily anisotropic heterogeneous medium. The gradient expressions were adapted for 2D VTI models, in which the in-plane polarized waves (P and SV) are controlled by combinations of four stiffness coefficients: C_{11}, C_{13}, C_{33}, and C_{55}.

To obtain radiation patterns for different model parameterizations, a point diffractor corresponding to a perturbation in the stiffness coefficients was inserted into a homogeneous isotropic background medium. By employing the Born and WKBJ approximations along with an asymptotic representation of the Green's functions, we derived a general expression for the Fréchet kernel of FWI. This result can be used to evaluate the sensitivity of the elastic FWI to parameters of arbitrarily anisotropic media.

The FWI algorithm and sensitivity analysis were implemented for two VTI model parameterizations. The first includes the P-wave vertical (V_{P0}), NMO (V_{nmo}), and horizontal (V_{hor}) velocities and the S-wave vertical velocity (V_{S0}). Parameterization II operates with the following parameter combinations: $\ln(1/V_{P0}^2)$, $\ln(1/V_{S0}^2)$, $(1+2\varepsilon)$, and $(1+2\delta)$. In both cases, the model parameters have the same order of magnitude, which makes it possible to update all of them using the same step-length in a given iteration. To gain insight into the potential of each parameterization, we obtained simple explicit expressions for the corresponding radiation patterns of P- and SV-waves.

For parameterization I, the scattered P-wavefield is insensitive to the S-wave velocity V_{S0}, whereas the radiation patterns of V_{P0} and V_{hor} are decoupled. An anomaly in V_{P0} scatters most of the P-wave energy in the vicinity of the symmetry axis, so stable estimation of V_{P0} requires good wavefield sampling in that range of angles. In contrast, a perturbation in V_{hor} produces the largest P-wave scattering near the isotropy (horizontal) plane, which helps estimate V_{hor} (and, therefore, ε) in crosshole geometry.

The SV-wavefield is not scattered by the velocity V_{P0}, so transmitted SV-waves cannot be used to invert for the P-wave symmetry-direction velocity. A perturbation in the shear-wave velocity V_{S0} scatters the SV-wave energy uniformly in all directions, thus allowing elastic FWI to recover V_{S0} for any aperture of the experiment. An anomaly in the velocity V_{nmo} predominantly scatters both the P- and SV-wavefields near an angle of 45°, and the scattering amplitude is smaller than that of the other parameters. Hence, transmitted P- and SV-waves do not provide tight constraints on the NMO velocity V_{nmo}, which could be estimated from reflected waves.

For parameterization II, an anomaly in V_{P0} scatters P-wave energy uniformly, whereas the radiation pattern of $1+2\varepsilon$ has the same shape as that for V_{hor} in parameterization I. Hence, this parameterization makes it possible to recover anomalies not just in ε, but also in V_{P0} for crosshole data. As is the case for parameterization I, V_{S0} is well constrained irrespective of the acquisition geometry.

Our results indicate that if the background model is known and the receivers record P- and SV-wave energy in the vicinity of the symmetry axis, FWI of transmission data using parameterization I should resolve the velocities V_{P0} and V_{S0}. In the case of crosshole geometry, multicomponent transmission data inverted with parameterization I constrain ε and V_{S0}. The main advantage of parameterization II is a uniform radiation pattern of the velocity V_{P0}, which helps estimate that parameter from crosshole data.

In the employed approximation, the radiation patterns of transmitted P-waves for elastic VTI media coincide with those for acoustic models. It is impossible, however, to estimate the velocity V_{S0} without including SV-waves. Also, when FWI is applied to more complex models and includes reflection data, the shear wavefield ought to provide tighter constraints on the velocities V_{P0}, V_{nmo}, and V_{hor}. If the wavefield is separated into P- and S-waves, it may be possible to apply a filter based on scattering angles to update a certain parameter (e.g., V_{S0} from shear data) or perform wavenumber filtering, as has been done for acoustic models.

ACKNOWLEDGMENTS

We are grateful to the members of the A(nisotropy) team at CWP, Tariq Alkhalifah (KAUST), and Andreas Rüger (Landmark Graphics) for fruitful discussions. Research reported in this publication was supported by the Consortium Project on Seismic Inverse Methods for Complex Structures at CWP, the CIMMM Project of the Unconventional Natural Gas Institute at CSM, and competitive research funding from King Abdullah University of Science and Technology (KAUST). The reproducible numeric examples in this paper are generated with the Madagascar open-source software package freely available from http://www.ahay.org.

APPENDIX A

GRADIENT COMPUTATION FOR VTI MEDIA USING THE ADJOINT-STATE METHOD

As discussed in Plessix (2006) and Liu and Tromp (2006), the objective function in equation 1 should be minimized under the constraint that the modeled displacement $\mathbf{u}(\mathbf{x}_r, t)$ satisfies the wave equation. Here, we use the elastic wave equation for heterogeneous, arbitrarily anisotropic media:

$$\rho \frac{\partial^2 u_i}{\partial t^2} - \frac{\partial}{\partial x_j}\left(c_{ijkl}\frac{\partial u_k}{\partial x_l}\right) = f_i, \tag{A-1}$$

where ρ is the density, c_{ijkl} are the components of the stiffness tensor, and $\mathbf{f}$ is the body force per unit volume. All indices range from 1 to 3 and summation over repeated indices is implied. The displacement wavefield is subject to the initial conditions,

$$\mathbf{u}(\mathbf{x},0)=0, \qquad \frac{\partial \mathbf{u}(\mathbf{x},0)}{\partial t}=0, \tag{A-2}$$

and the radiation boundary condition,

$$\mathbf{u}(\mathbf{x},t)|_{\mathbf{x}\to\infty}\to 0. \tag{A-3}$$

The method of Lagrange multipliers (Strang, 1991) is used to define the Lagrangian Λ:

$$\Lambda=\frac{1}{2}\sum_r \|\mathbf{u}(\mathbf{x}_r,t)-\mathbf{d}(\mathbf{x}_r,t)\|^2 - \int_0^T\int_\Omega \lambda_i\left[\rho\frac{\partial^2 u_i}{\partial t^2}-\frac{\partial}{\partial x_j}\left(c_{ijkl}\frac{\partial u_k}{\partial x_l}\right)-f_i\right]dVdt, \tag{A-4}$$

where $r=1,2\ldots N$ denotes the receivers, Ω is the integration domain (which includes the entire 3D space), $\partial\Omega$ is the surface of Ω, and $\boldsymbol{\lambda}(\mathbf{x},t)$ is the vector Lagrange multiplier that needs to be determined. The objective is to find the stationary points of the Lagrangian, which is done by calculating the variation in Λ when $\mathbf{u}$, $\boldsymbol{\lambda}$, and c_{ijkl} are perturbed. After integration by parts and application of the Gauss divergence theorem, we obtain the change in the Lagrangian,

$$\begin{aligned}\delta\lambda=&\int_0^t\int_\omega\sum_{r=1}^{n}[u_i(\mathbf{x},t)-d_i(\mathbf{x},t)]\delta(\mathbf{x}-\mathbf{x}_r)\delta u_i\ dvdt\\ &-\int_0^t\int_\omega \delta c_{ijkl}\frac{\partial u_k}{\partial x_l}\frac{\partial\lambda_i}{\partial x_j}dvdt\\ &-\int_0^t\int_\omega\left[\rho\frac{\partial^2\lambda_i}{\partial t^2}-\frac{\partial}{\partial x_j}\left(c_{ijkl}\frac{\partial\lambda_k}{\partial x_l}\right)\right]\delta u_i\ dvdt\\ &-\int_0^t\int_\omega\left[\rho\frac{\partial^2\lambda_i}{\partial t^2}-\frac{\partial}{\partial x_j}\left(c_{ijkl}\frac{\partial\lambda_k}{\partial x_l}\right)-f_i\right]\delta\lambda_i\ dvdt\\ &-\int_\omega\left[\rho\lambda_i\frac{\partial(\delta u_i)}{\partial t}-\rho\,(\delta u_i)\ \frac{\partial\lambda_i}{\partial t}\right]\Big|_0^t dv\\ &+\int_0^t\int_{\partial\omega}\lambda_i\left[\delta c_{ijkl}\frac{\partial u_k}{\partial x_l}+c_{ijkl}\frac{\partial(\delta u_k)}{\partial x_l}\right]n_j\ ds\ dt\\ &-\int_0^t\int_{\partial\omega}\delta u_i\ c_{ijkl}\frac{\partial\lambda_k}{\partial x_l}\ n_j\ ds\ dt,\end{aligned} \tag{A-5}$$

where $\mathbf{n}$ is the vector normal to the surface $\partial\Omega$. Perturbing $\mathbf{u}(\mathbf{x},t)$ in equations A-2 and A-3 yields the initial and boundary conditions for $\delta\mathbf{u}(\mathbf{x},t)$:

$$\delta\mathbf{u}(\mathbf{x},0)=0, \quad \frac{\partial[\delta\mathbf{u}(\mathbf{x},t)]}{\partial t}=0, \quad \delta\mathbf{u}(\mathbf{x},t)|_{\mathbf{x}\to\infty}\to 0. \tag{A-6}$$

The Lagrange multiplier $\boldsymbol{\lambda}$ is constrained by the "final" conditions (i.e., those at time T),

$$\boldsymbol{\lambda}(\mathbf{x},T)=0, \quad \frac{\partial\boldsymbol{\lambda}(\mathbf{x},T)}{\partial t}=0, \tag{A-7}$$

and the boundary condition,

$$\boldsymbol{\lambda}(\mathbf{x},t)|_{\mathbf{x}\to\infty}\to 0. \tag{A-8}$$

Equation A-5 then reduces to

$$\begin{aligned}\delta\lambda=&\int_0^t\int_\omega\left\{\sum_{r=1}^{n}(u_i(\mathbf{x},t)-d_i(\mathbf{x},t))\delta(\mathbf{x}-\mathbf{x}_r)\right.\\ &\left.-\left[\rho\frac{\partial^2\lambda_i}{\partial t^2}-\frac{\partial}{\partial x_j}\left(c_{ijkl}\frac{\partial\lambda_k}{\partial x_l}\right)\right]\right\}\delta u_i\ \ dv\,dt\\ &-\int_0^t\int_\omega\frac{\partial u_k}{\partial x_l}\frac{\partial\lambda_i}{\partial x_j}\delta\ c_{ijkl}\ \ dv\,dt\\ &-\int_0^t\int_\omega\left[\rho\frac{\partial^2\lambda_i}{\partial t^2}-\frac{\partial}{\partial x_j}\left(c_{ijkl}\frac{\partial\lambda_k}{\partial x_l}\right)-f_i\right]\delta\lambda_i\ \ dv\,dt.\end{aligned} \tag{A-9}$$

The Lagrangian is stationary with respect to the variables $\mathbf{u}$, $\boldsymbol{\lambda}$, and c_{ijkl} when the coefficients of δu_i, $\delta\lambda_i$, and δc_{ijkl} in the integrands of equation A-9 go to zero. For a given model (i.e., fixed c_{ijkl}), setting the coefficient of $\delta\lambda_i$ to zero gives the state equation, which coincides with the elastic wave equation A-1. Setting the coefficient of δu_i to zero yields the adjoint-state equation:

$$\rho\frac{\partial^2\lambda_i}{\partial t^2}-\frac{\partial}{\partial x_j}\left(c_{ijkl}\frac{\partial\lambda_k}{\partial x_l}\right)=\sum_{r=1}^{N}\ \left[u_i(\mathbf{x}_r,t)-d_i(\mathbf{x}_r,t)\right], \tag{A-10}$$

subject to the conditions at time T (equation A-7) and boundary conditions (equation A-8). Equations A-1 and then A-10 are solved to obtain the wavefields $\mathbf{u}$ and $\boldsymbol{\lambda}$ respectively.

Substituting $\mathbf{u}$ and $\boldsymbol{\lambda}$ into the coefficient of the term containing δc_{ijkl} in equation A-9 gives the variation in the Lagrangian with the stiffnesses. Since $\Lambda=\mathcal{F}$ when $\mathbf{u}$ satisfies the wave equation (from equation A-4), the change in the objective function $\delta\mathcal{F}$ caused by perturbations of the stiffness coefficients is given by:

$$\delta\mathcal{F}=-\int_0^T\int_\Omega\frac{\partial u_i}{\partial x_j}\frac{\partial\lambda_k}{\partial x_l}\,\delta c_{ijkl}\ dVdt. \tag{A-11}$$

This is a general result for an anisotropic medium described by the complete stiffness tensor c_{ijkl}. Expressions for models with specific symmetries can be derived from equation A-11 by substituting the appropriate stiffness tensors or matrices.

Note that the boundary conditions for $\mathbf{u}(\mathbf{x},t)$ and $\boldsymbol{\lambda}(\mathbf{x},t)$ can be modified to include a free surface where the tractions due to $\mathbf{u}$ and $\boldsymbol{\lambda}$ go to zero. However, the addition of the free surface causes

complications in finite-difference modeling and produces surface multiples. Instead, we impose the radiation condition to create absorbing boundaries on all sides of the model.

To simulate the Lagrange-multiplier wavefield, it is convenient to define an "adjoint wavefield" $\boldsymbol{\psi}$ (Liu and Tromp, 2006):

$$\boldsymbol{\psi}(\mathbf{x},t)\equiv\lambda(\mathbf{x},T-t). \tag{A-12}$$

The wavefield $\boldsymbol{\psi}$ satisfies the wave equation A-10 but with the source function reversed in time:

$$\rho\frac{\partial^2\psi_i}{\partial t^2}-\frac{\partial}{\partial x_j}\left(c_{ijkl}\frac{\partial\psi_k}{\partial x_l}\right)=\sum_{r=1}^{N}[u_i(\mathbf{x}_r,T-t)-d_i(\mathbf{x}_r,T-t)]. \tag{A-13}$$

The initial conditions for $\boldsymbol{\psi}$ (using equations A-7 and A-12) are as follows:

$$\boldsymbol{\psi}(\mathbf{x},0)=0,\qquad\frac{\partial\boldsymbol{\psi}(\mathbf{x},0)}{\partial t}=0. \tag{A-14}$$

The wavefield $\boldsymbol{\psi}$ also satisfies the radiation boundary condition:

$$\boldsymbol{\psi}(\mathbf{x},t)|_{\mathbf{x}\to\infty}\to 0. \tag{A-15}$$

From equations A-11 and A-12, we can find the gradient of the objective function with respect to the stiffness coefficients:

$$\frac{\partial\mathcal{F}}{\partial c_{ijkl}}=-\int_0^T\frac{\partial u_i}{\partial x_j}\frac{\partial\psi_k}{\partial x_l}dt. \tag{A-16}$$

If, instead of c_{ijkl}, the model is described by parameters m_n, the gradient of $\mathcal{F}$ can be found from the chain rule:

$$\frac{\partial\mathcal{F}}{\partial m_n}=\sum_{ijkl}\frac{\partial\mathcal{F}}{\partial c_{ijkl}}\frac{\partial c_{ijkl}}{\partial m_n}. \tag{A-17}$$

Here, we implement FWI for two sets of parameters. First, the model is parameterized in terms of the velocities V_{P0}, V_{S0}, V_{nmo}, and V_{hor}. The stiffness coefficients (written in the two-index notation) represent the following functions of the velocities (Tsvankin, 2012):

$$C_{11}=\rho V_{\mathrm{hor}}^2, \tag{A-18}$$

$$C_{33}=\rho V_{P0}^2, \tag{A-19}$$

$$C_{13}=\rho\sqrt{(V_{P0}^2-V_{S0}^2)(V_{\mathrm{nmo}}^2-V_{S0}^2)}-\rho V_{S0}^2, \tag{A-20}$$

$$C_{55}=\rho V_{S0}^2. \tag{A-21}$$

Using equations A-16, A-17, and A-18–A-21, we obtain the derivatives of the objective function with respect to the velocities:

$$\frac{\partial\mathcal{F}}{\partial V_{P0}}=-2\rho V_{P0}\int_0^T\left[\frac{\partial\psi_3}{\partial x_3}\frac{\partial u_3}{\partial x_3}+\frac{1}{2}\sqrt{\frac{V_{\mathrm{nmo}}^2-V_{S0}^2}{V_{P0}^2-V_{S0}^2}}\left(\frac{\partial\psi_1}{\partial x_1}\frac{\partial u_3}{\partial x_3}+\frac{\partial\psi_3}{\partial x_3}\frac{\partial u_1}{\partial x_1}\right)\right]dt, \tag{A-22}$$

$$\frac{\partial\mathcal{F}}{\partial V_{S0}}=-2\rho V_{S0}\int_0^T\left\{\left[\frac{2V_{S0}^2-V_{P0}^2-V_{\mathrm{nmo}}^2}{2\sqrt{(V_{\mathrm{nmo}}^2-V_{S0}^2)(V_{P0}^2-V_{S0}^2)}}-1\right]\left(\frac{\partial\psi_1}{\partial x_1}\frac{\partial u_3}{\partial x_3}+\frac{\partial\psi_3}{\partial x_3}\frac{\partial u_1}{\partial x_1}\right)+\left(\frac{\partial\psi_1}{\partial x_3}+\frac{\partial\psi_3}{\partial x_1}\right)\left(\frac{\partial u_1}{\partial x_3}+\frac{\partial u_3}{\partial x_1}\right)\right\}dt, \tag{A-23}$$

$$\frac{\partial\mathcal{F}}{\partial V_{\mathrm{nmo}}}=-\rho V_{\mathrm{nmo}}\int_0^T\sqrt{\frac{V_{P0}^2-V_{S0}^2}{V_{\mathrm{nmo}}^2-V_{S0}^2}}\left(\frac{\partial\psi_1}{\partial x_1}\frac{\partial u_3}{\partial x_3}+\frac{\partial\psi_3}{\partial x_3}\frac{\partial u_1}{\partial x_1}\right)dt, \tag{A-24}$$

$$\frac{\partial\mathcal{F}}{\partial V_{\mathrm{hor}}}=-2\rho V_{\mathrm{hor}}\int_0^T\frac{\partial\psi_1}{\partial x_1}\frac{\partial u_1}{\partial x_1}dt. \tag{A-25}$$

The second parameterization includes the following parameters (after Shen, 2012):

$$m_1=\ln\left(\frac{1}{V_{P0}^2}\right), \tag{A-26}$$

$$m_2=\ln\left(\frac{1}{V_{S0}^2}\right), \tag{A-27}$$

$$m_3=1+2\varepsilon, \tag{A-28}$$

$$m_4=1+2\delta. \tag{A-29}$$

After the stiffness coefficients are expressed in terms of m_1, m_2, m_3, and m_4, equations A-16 and A-17 yield:

$$\frac{\partial\mathcal{F}}{\partial m_1}=\rho V_{P0}^2\int_0^T\left\{(1+2\varepsilon)\frac{\partial\psi_1}{\partial x_1}\frac{\partial u_1}{\partial x_1}+\frac{\partial\psi_3}{\partial x_3}\frac{\partial u_3}{\partial x_3}+\left[\frac{f}{2}(1+2\delta)+\frac{1}{2f}\right]\left(\frac{\partial\psi_3}{\partial x_3}\frac{\partial u_1}{\partial x_1}+\frac{\partial\psi_1}{\partial x_1}\frac{\partial u_3}{\partial x_3}\right)\right\}dt, \tag{A-30}$$

$$\frac{\partial\mathcal{F}}{\partial m_2}=\rho V_{S0}^2\int_0^T\left[\left(\frac{\partial\psi_1}{\partial x_3}+\frac{\partial\psi_3}{\partial x_1}\right)\left(\frac{\partial u_1}{\partial x_3}+\frac{\partial u_3}{\partial x_1}\right)-\left(\frac{f}{2}+\frac{1}{2f}+1\right)\left(\frac{\partial\psi_3}{\partial x_3}\frac{\partial u_1}{\partial x_1}+\frac{\partial\psi_1}{\partial x_1}\frac{\partial u_3}{\partial x_3}\right)\right]dt, \tag{A-31}$$

$$\frac{\partial \mathcal{F}}{\partial m_3} = -\rho V_{P0}^2 \int_0^T \frac{\partial \psi_1}{\partial x_1}\frac{\partial u_1}{\partial x_1} dt, \tag{A-32}$$

$$\frac{\partial \mathcal{F}}{\partial m_4} = -\rho V_{P0}^2 \frac{f}{2} \int_0^T \left(\frac{\partial \psi_3}{\partial x_3}\frac{\partial u_1}{\partial x_1} + \frac{\partial \psi_1}{\partial x_1}\frac{\partial u_3}{\partial x_3}\right) dt, \tag{A-33}$$

where

$$f \equiv \sqrt{\frac{V_{P0}^2 - V_{S0}^2}{(1+2\delta)V_{P0}^2 - V_{S0}^2}}. \tag{A-34}$$

APPENDIX B

SENSITIVITY PATTERNS FOR ELASTIC FWI IN VTI MEDIA

The radiation pattern is obtained by expressing the scattered wavefield in the Born approximation using the asymptotic Green's function.

Suppose the wavefield produced by a source at location $\mathbf{x}_s$ is scattered at $\mathbf{x}'$ and recorded by a receiver at $\mathbf{x}_r$. A perturbation δc_{ijkl} in the stiffness coefficient c_{ijkl} at the scatterer $\mathbf{x}'$ (Figure B-1) results in a perturbation δu_i in the wavefield. We replace the wavefield u_i in equation A-1 by $u_i = u_i^b + \delta u_i$ and the stiffnesses c_{ijkl} by $c_{ijkl} = c_{ijkl}^b + \delta c_{ijkl}$, where the superscript b refers to the background medium. Retaining only the terms linear in the perturbations in equation A-1 leads to the Born approximation:

$$\rho\frac{\partial^2(\delta u_i)}{\partial t^2} - \frac{\partial}{\partial x_j}\left(c_{ijkl}^b \frac{\partial(\delta u_k)}{\partial x_l}\right) = \frac{\partial}{\partial x_j}\left(\delta c_{ijkl}\frac{\partial u_k^b}{\partial x_l}\right). \tag{B-1}$$

The wave equation A-1 can be solved in the frequency domain in terms of the Green's function using the representation theorem:

$$u_n(\mathbf{x}_r,\omega) = \int_{V(\mathbf{x}')} h_i(\mathbf{x}',\omega)\; G_{ni}(\mathbf{x}_r,\mathbf{x}',\omega) dV(\mathbf{x}'), \tag{B-2}$$

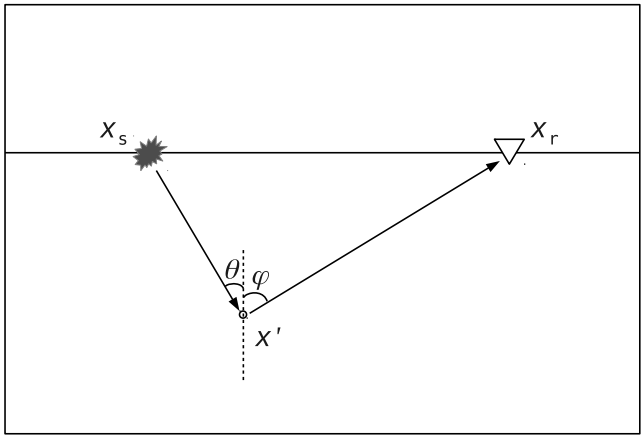

Figure B-1. Geometry of the scattering experiment. The source is located at $\mathbf{x}_s$, the scatterer at $\mathbf{x}'$, and the receiver at $\mathbf{x}_r$.

where $h_i(\mathbf{x}',\omega)$ is the force density at $\mathbf{x}'$, $G_{ni}(\mathbf{x}_r,\mathbf{x}',\omega)$ is the Green's function for the source at $\mathbf{x}'$ and receiver at $\mathbf{x}_r$, and $V(\mathbf{x}')$ represents the volume that includes all sources. To solve equation B-1 for the scattered field, we replace $h_i(\mathbf{x}',\omega)$ in equation B-2 by the right-hand side (source term) of equation B-1:

$$\begin{aligned}\delta u_n(\mathbf{x}_r,\omega) &= \int_{V(\mathbf{x}')} \frac{\partial}{\partial x_j'}\left(\delta c_{ijkl}\frac{\partial u_k^b}{\partial x_l'}\right) G_{ni}\, dV(\mathbf{x}') \\ &= \int_{V(\mathbf{x}')} \left[\frac{\partial}{\partial x_j'}(\delta c_{ijkl}\frac{\partial u_k^b}{\partial x_l'}G_{ni}) - \delta c_{ijkl}\frac{\partial u_k^b}{\partial x_l'}\frac{\partial G_{ni}}{\partial x_j'}\right] dV(\mathbf{x}').\end{aligned} \tag{B-3}$$

Applying the divergence theorem to the first term in the integrand of equation B-3 yields:

$$\begin{aligned}\delta u_n(\mathbf{x}_r,\omega) = &\int_{S(\mathbf{x}')} \delta c_{ijkl}\frac{\partial u_k^b}{\partial x_l'} G_{ni}\;\nu_j\; dS(\mathbf{x}') \\ &- \int_{V(\mathbf{x}')} \delta c_{ijkl}\frac{\partial u_k^b}{\partial x_l'}\frac{\partial G_{ni}}{\partial x_j'} dV(\mathbf{x}'),\end{aligned} \tag{B-4}$$

where $S(\mathbf{x}')$ is the surface of the volume $V(\mathbf{x}')$, and ν is the normal to $S(\mathbf{x}')$ pointing outward. Expanding the volume $V(\mathbf{x}')$ to infinity and using the radiation boundary condition (equation A-3) reduces equation B-4 to

$$\delta u_n(\mathbf{x}_r,\omega) = -\int_{V(\mathbf{x}')} \delta c_{ijkl}(\mathbf{x}')\frac{\partial u_k^b(\mathbf{x}',\omega)}{\partial x_l'}\frac{\partial G_{ni}(\mathbf{x}_r,\mathbf{x}',\omega)}{\partial x_j'} dV(\mathbf{x}'). \tag{B-5}$$

Here, the wavefield $\mathbf{u}^b$ is computed in the background medium and is generated by the force at the source location $\mathbf{x}_s$. Hence, $\mathbf{u}^b$ can be expressed in terms of the force applied at $\mathbf{x}_s$ and the Green's function:

$$u_k^b(\mathbf{x}',\omega) = f_m(\mathbf{x}_s,\omega)\; G_{km}(\mathbf{x}',\mathbf{x}_s,\omega). \tag{B-6}$$

Substituting equation B-6 into equation B-4 and using reciprocity,

$$G_{km}(\mathbf{x}',\mathbf{x}_s,\omega) = G_{mk}(\mathbf{x}_s,\mathbf{x}',\omega), \tag{B-7}$$

we find:

$$\begin{aligned}\delta u_n(\mathbf{x}_r,\omega) = &-\int_{V(\mathbf{x}')} f_m(\mathbf{x}_s,\omega)\delta c_{ijkl}(\mathbf{x}') \\ &\times\frac{\partial G_{mk}(\mathbf{x}_s,\mathbf{x}',\omega)}{\partial x_l'}\frac{\partial G_{ni}(\mathbf{x}_r,\mathbf{x}',\omega)}{\partial x_j'} dV(\mathbf{x}').\end{aligned} \tag{B-8}$$

Next, we assume the background medium to be homogeneous (it can still be arbitrarily anisotropic). The Green's functions in equation B-8 can be replaced by their asymptotic (high-frequency) representation (Vavryčuk, 2007),

$$G_{mk} = g_m^s\; g_k^s\; \bar{G}^s, \tag{B-9}$$

$$G_{ni} = g_n^r\; g_i^r\; \bar{G}^r, \tag{B-10}$$

where the superscripts s and r denote the source and receiver wavefields, respectively, $\mathbf{g}$ is the unit polarization vector, and

$$\bar{G}^s = \frac{1}{4\pi\rho V^s_{gr} R^s \sqrt{|K|}} \exp\left[i\frac{\pi}{2}\sigma_0 + i\omega\frac{\mathbf{p}^s}{v^s}\cdot(\mathbf{x}^s - \mathbf{x}')\right], \tag{B-11}$$

$$\bar{G}^r = \frac{1}{4\pi\rho V^r_{gr} R^r \sqrt{|K|}} \exp\left[i\frac{\pi}{2}\sigma_0 + i\omega\frac{\mathbf{p}^r}{v^r}\cdot(\mathbf{x}^r - \mathbf{x}')\right]. \tag{B-12}$$

Here, V_{gr} and R are the group velocity and distance along the ray (the rays connect the scatterer with the source and receiver), K is the Gaussian curvature of the slowness surface, σ_0 is a function of K (Vavryčuk, 2007), $\mathbf{p}$ is the unit slowness vector, and v is the phase velocity.

In the WKBJ approximation (e.g., Aki and Richards, 2002), the spatial derivatives are evaluated only for the rapidly varying terms of the Greens's function (i.e., the exponents in equations B-11 and B-12). Substituting equations B-9–B-12 into equation B-8 yields the following expression for the perturbed wavefield:

$$\delta u_n(\mathbf{x}_r,\omega) = \int_{V(\mathbf{x}')} f_m(\mathbf{x}_s,\omega)\ \mathcal{A}(\omega)\ p^s_l\, p^r_j\, g^s_k\, g^r_i\, \delta c_{ijkl}\, dV(\mathbf{x}'), \tag{B-13}$$

where

$$\mathcal{A}(\omega) = g^s_m\, g^r_n\, \bar{G}^s \bar{G}^r\, \frac{\omega^2}{v^s v^r}. \tag{B-14}$$

The "radiation pattern" Ω for a model parameterized in terms of the stiffnesses is obtained as the amplitude of the kernel (Alkhalifah and Plessix, 2014) in equation B-13 (i.e., the coefficient multiplied with δc_{ijkl}):

$$\Omega = p^s_l\, p^r_j\, g^s_k\, g^r_i. \tag{B-15}$$

This is a general expression for an arbitrarily anisotropic scatterer embedded in a homogeneous anisotropic background.

Next, we assume the background to be isotropic, and the scatterer to be defined by the stiffness coefficients corresponding to the P- and SV-waves in VTI media (i.e., C_{11}, C_{13}, C_{33}, and C_{55}). Equations A-18–A-21 allow us to calculate the total differential for each stiffness element C_{ij} with respect to the independent variables (V_{P0}, V_{S0}, V_{nmo}, and V_{hor}) and substitute them into equation B-13. We can thus obtain the perturbation for each velocity (V_{P0}, V_{S0}, V_{nmo}, and V_{hor}). Since the background medium is isotropic, the background velocities V_{nmo}, V_{hor}, and V_{P0} are equal, and the unit polarization vectors are parallel (P-waves) or perpendicular (SV-waves) to the corresponding group-velocity vector. For the P-wavefield, the 2D radiation patterns (for parameterization I) in the vertical plane take the form:

$$\Omega^P(V_{P0}) = 2\rho V_{P0}[2(p^s_3)^2\ (p^r_3)^2 + (p^s_3)^2\ (p^r_1)^2 + (p^s_1)^2\ (p^r_3)^2], \tag{B-16}$$

$$\Omega^P(V_{S0}) = 8\rho\, V_{S0}[2p^s_1\, p^s_3\, p^r_1\, p^r_3 - (p^s_3)^2\ (p^r_1)^2 - (p^s_1)^2\ (p^r_3)^2], \tag{B-17}$$

$$\Omega^P(V_{\mathrm{nmo}}) = 2\rho V_{P0}[(p^s_3)^2\ (p^r_1)^2 + (p^s_1)^2\ (p^r_3)^2], \tag{B-18}$$

$$\Omega^P(V_{\mathrm{hor}}) = 4\rho\, V_{P0}(p^s_1)^2\ (p^r_1)^2. \tag{B-19}$$

The patterns for the S-wavefield are:

$$\Omega^S(V_{P0}) = 0, \tag{B-20}$$

$$\Omega^S(V_{S0}) = 4\rho V_{S0}[(p^s_1 p^r_1 + p^s_3 p^r_3)^2 - (p^s_1 p^r_3 - p^s_3 p^r_1)^2], \tag{B-21}$$

$$\Omega^S(V_{\mathrm{nmo}}) = -4\rho V_{P0}\, p^s_1\, p^s_3\, p^r_1\, p^r_3, \tag{B-22}$$

$$\Omega^S(V_{\mathrm{hor}}) = 4\rho V_{P0}\, p^s_1\, p^s_3\, p^r_1\, p^r_3. \tag{B-23}$$

For transmitted waves, the incident and scattering angles are the same, and the components of the unit slowness and polarization vectors for P-waves become:

$$p^1_s = g^1_s = -\sin\theta, \tag{B-24}$$

$$p^3_s = g^3_s = \cos\theta, \tag{B-25}$$

$$p^1_r = g^1_r = \sin\theta, \tag{B-26}$$

$$p^3_r = g^3_r = -\cos\theta, \tag{B-27}$$

where θ is the phase angle with the (vertical) symmetry axis. For SV-waves, the corresponding expressions are:

$$p^1_s = -g^3_s = -\sin\theta, \tag{B-28}$$

$$p^3_s = g^1_s = \cos\theta, \tag{B-29}$$

$$p^1_r = g^3_r = \sin\theta, \tag{B-30}$$

$$p^3_r = -g^1_r = -\cos\theta. \tag{B-31}$$

The final expressions for the P- and S-wave radiation patterns are given in the main text. The radiation patterns for parameterization II [$\ln(1/V^2_{P0})$, $\ln(1/V^2_{S0})$, $1+2\varepsilon$, and $1+2\delta$] are obtained in a similar manner.

REFERENCES

Aki, K., and P. G. Richards, 2002, Quantitative seismology, 2nd ed.: University Science Books.

Alkhalifah, T., and R. Plessix, 2014, A recipe for practical full-waveform inversion in anisotropic media: An analytical parameter resolution study: Geophysics, **79**, no. 3, R91–R101, doi: 10.1190/geo2013-0366.1.

Alkhalifah, T., and I. Tsvankin, 1995, Velocity analysis for transversely isotropic media: Geophysics, **60**, 1550–1566, doi: 10.1190/1.1443888.

Bamberger, A., G. Chavent, C. Hemon, and P. Lailly, 1982, Inversion of normal incidence seismograms: Geophysics, **47**, 757–770, doi: 10.1190/1.1441345.

Bunks, C., F. M. Saleck, S. Zaleski, and G. Chavent, 1995, Multiscale seismic waveform inversion: Geophysics, **60**, 1457–1473, doi: 10.1190/1.1443880.

Calvet, M., S. Chevrot, and A. Souriau, 2006, P-wave propagation in transversely isotropic media: I — Finite-frequency theory: Physics of the Earth and Planetary Interiors, **156**, 12–20, doi: 10.1016/j.pepi.2006.01.004.

Eaton, D. W. S., and R. R. Stewart, 1994, Migration/inversion for transversely isotropic elastic media: Geophysical Journal International, **119**, 667–683, doi: 10.1111/j.1365-246X.1994.tb00148.x.

Fichtner, A., H.-P. Bunge, and H. Igel, 2006, The adjoint method in seismology: I — Theory: Physics of the Earth and Planetary Interiors, **157**, 86–104, doi: 10.1016/j.pepi.2006.03.016.

Gauthier, O., 1986, Two-dimensional nonlinear inversion of seismic waveforms: Numerical results: Geophysics, **51**, 1387–1403, doi: 10.1190/1.1442188.

Gholami, Y., R. Brossier, S. Operto, V. Prieux, A. Ribodetti, and J. Virieux, 2011, Two-dimensional acoustic anisotropic (VTI) full waveform inversion: The Valhall case study: 81st Annual International Meeting, SEG, Expanded Abstracts, 2543–2548.

Gholami, Y., R. Brossier, S. Operto, A. Ribodetti, and J. Virieux, 2013, Which parameterization is suitable for acoustic vertical transverse isotropic full waveform inversion? Part 1: Sensitivity and trade-off analysis: Geophysics, **78**, no. 2, R81–R105, doi: 10.1190/geo2012-0204.1.

Kamath, N., and I. Tsvankin, 2013, Full-waveform inversion of multicomponent data for horizontally layered VTI media: Geophysics, **78**, no. 2, WC113–WC121, doi: 10.1190/geo2012-0415.1.

Kolb, P., F. Collino, and P. Lailly, 1986, Pre-stack inversion of a 1-D medium: Proceedings of the IEEE, **74**, 498–508, doi: 10.1109/PROC.1986.13490.

Lee, H., J. M. Koo, D. Min, B. Kwon, and H. S. Yoo, 2010, Frequency-domain elastic full waveform inversion for VTI media: Geophysical Journal International, **183**, 884–904, doi: 10.1111/j.1365-246X.2010.04767.x.

Liu, Q., and J. Tromp, 2006, Finite-frequency kernels based on adjoint methods: Bulletin of the Seismological Society of America, **96**, 2383–2397, doi: 10.1785/0120060041.

Mora, P., 1987, Nonlinear two-dimensional elastic inversion of multioffset seismic data: Geophysics, **52**, 1211–1228, doi: 10.1190/1.1442384.

Plessix, R., 2006, A review of the adjoint-state method for computing the gradient of a functional with geophysical applications: Geophysical Journal International, **167**, 495–503, doi: 10.1111/j.1365-246X.2006.02978.x.

Plessix, R., and Q. Cao, 2011, A parameterization study for surface seismic full waveform inversion in an acoustic vertical transversely isotropic medium: Geophysical Journal International, **185**, 539–556, doi: 10.1111/j.1365-246X.2011.04957.x.

Plessix, R.-E., and H. Rynja, 2010, VTI full waveform inversion: A parameterization study with a narrow azimuth streamer data example: 80th Annual International Meeting, SEG, Expanded Abstracts, 962–966.

Pratt, G., C. Shin, and Hicks, 1998, Gauss-Newton and full Newton methods in frequency-space seismic waveform inversion: Geophysical Journal International, **133**, 341–362, doi: 10.1046/j.1365-246X.1998.00498.x.

Pratt, R. G., 1999, Seismic waveform inversion in the frequency domain, Part 1: Theory and verification in a physical scale model: Geophysics, **64**, 888–901, doi: 10.1190/1.1444597.

Pratt, R. G., and R. M. Shipp, 1999, Seismic waveform inversion in the frequency domain, Part 2: Fault delineation in sediments using crosshole data: Geophysics, **64**, 902–914, doi: 10.1190/1.1444598.

Prieux, V., R. Brossier, Y. Gholami, S. Operto, J. Virieux, O. I. Barkved, and J. H. Kommedal, 2011, On the footprint of anisotropy on isotropic full waveform inversion: The Valhall case study: Geophysical Journal International, **187**, 1495–1515, doi: 10.1111/j.1365-246X.2011.05209.x.

Prieux, V., R. Brossier, S. Operto, and J. Virieux, 2013, Multiparameter full waveform inversion of multicomponent ocean-bottom-cable data from the Valhall field, Part 1: Imaging compressional wave speed, density and attenuation: Geophysical Journal International, **194**, 1640–1664, doi: 10.1093/gji/ggt177.

Shen, X., 2012, Early-arrival waveform inversion for near-surface velocity and anisotropic parameter: Parametrization study: 82nd Annual International Meeting, SEG, Expanded Abstracts, doi: 10.1190/segam2012-0730.1.

Song, Z., and P. R. Williamson, 1995, Frequency-domain acoustic-wave modeling and inversion of crosshole data, Part 1: 2.5-D modeling method: Geophysics, **60**, 784–795, doi: 10.1190/1.1443817.

Song, Z., P. R. Williamson, and R. G. Pratt, 1995, Frequency-domain acoustic-wave modeling and inversion of crosshole data: Part II, inversion method, synthetic experiments and real-data results: Geophysics, **60**, 796–809, doi: 10.1190/1.1443818.

Strang, G., 1991, Calculus: Wellesley-Cambridge Press.

Tarantola, A., 1984a, Inversion of seismic reflection data in the acoustic approximation: Geophysics, **49**, 1259–1266, doi: 10.1190/1.1441754.

Tarantola, A., 1984b, Linearized inversion of seismic reflection data: Geophysical Prospecting, **32**, 998–1015, doi: 10.1111/j.1365-2478.1984.tb00751.x.

Tsvankin, I., 2012, Seismic signatures and analysis of reflection data in anisotropic media, 3rd ed.: SEG.

Vavryčuk, V., 2007, Asymptotic Green's function in homogeneous anisotropic viscoelastic media: Proceedings of the Royal Society A: Mathematical, Physical and Engineering Science, **463**, 2689–2707, doi: 10.1098/rspa.2007.1862.

Virieux, J., and S. Operto, 2009, An overview of full-waveform inversion in exploration geophysics: Geophysics, **74**, no. 6, WCC1–WCC26, doi: 10.1190/1.3238367.

Warner, M., A. Ratcliffe, T. Nangoo, J. Morgan, A. Umpleby, N. Shah, V. Vinje, I. Tekl, L. Guasch, C. Win, G. Conroy, and A. Bertrand, 2013, Anisotropic 3D full-waveform inversion: Geophysics, **78**, no. 2, R59–R80, doi: 10.1190/geo2012-0338.1.

Wu, R., and M. Toksöz, 1987, Diffraction tomography and multisource holography applied to seismic imaging: Geophysics, **52**, 11–25, doi: 10.1190/1.1442237.